Using Daily Observations from Planet Labs Satellite Imagery to Separate the Surface Deformation Between the July 4th M_w 6.4 Foreshock and July 5th M_w 7.1 Mainshock During the 2019 Ridgecrest Earthquake Sequence.

Author list: Chris Milliner[1], Andrea Donnellan[1]

1. Jet Propulsion Laboratory, California Institute of Technology, CA 91109

Abstract

On July 4th 2019 the Ridgecrest earthquake sequence began with a series of foreshocks including a M_w 6.4 event near Searles Valley, California. This was then followed 34 hours later by a M_w 7.1 mainshock located just 15 km to the north, with the earthquake sequence resulting in a complex array of intersecting faults. This earthquake sequence poses several interesting questions including, did the stress changes induced by the M_w 6.4 foreshock trigger the M_w 7.1 mainshock and what possible mechanism(s) could explain the occurrence of widespread secondary faulting surrounding both surface ruptures? However, most of the geodetic data (such as InSAR, lidar and optical satellite imagery), were acquired after both events had occurred making it difficult to discern which surface fractures happened when and their possible triggering mechanism. Here we provide a dataset composed of high-resolution optical imagery, pixel-value difference maps, .kmz fracturing mapping and horizontal deformation maps derived from subpixel image correlation, which can uniquely separate the surface fracturing and deformation between the foreshock and mainshock events that can help answer these questions. Separate imaging of the events is made possible by

the daily acquisition of optical imagery by the Planet labs cubesat constellation, which acquired data between the two earthquakes, on the morning of July 4^{th} and 5^{th}, at 11.13 am and 17.12 pm PST, respectively, with the images acquired just 40 minutes after the foreshock and 56 minutes before the mainshock, respectively. Analysis from these optical imagery reveals the location of surface faulting that allow us to map their spatial extent and determine their timing. These data which we provide here can help guide and validate field survey observations to help understand which faults ruptured when, and constrain slip inversion models for more accurate estimates of stress changes induced by the foreshock imposed on the surrounding faults.

Keywords: Ridgecrest, surface deformation, fractures, displacement, triggering

Introduction

The 2019 Ridgecrest earthquake sequence initiated on the morning of July 4^{th}, ~15 km east of the city of Ridgecrest, California, within the Eastern California Shear Zone (ECSZ), a 160 km wide region of NW-trending dextral shearing that accommodates ~10-20% of the Pacific-North America plate boundary motion (McClusky et al., 2001; Rockwell et al., 2000). This region has hosted three historical major events including the 1873 Owens valley earthquake located 45 km to the north of the Ridgecrest rupture, and the 1992 M_w 7.3 Landers and 1999 M_w 7.1 Hector Mine ruptures both located ~110 km to the SE in the Mojave Desert. The Ridgecrest earthquake sequence begun with a series of foreshocks that preceded a M_w 6.4 event which occurred at 10.33 am PST on July 4^{th}, south of China Lake that was mostly left-lateral, but possibly also involved rupture of north-west striking right-lateral faults (Fig. 1) (Chen et al., 2019). This was then followed by a series of aftershocks (now designated as foreshocks to the mainevent), including a M_w 5.0, and a M_w 5.4 on July 5th, at 4.07 pm, and 8.16 pm PST, respectively, that migrated along a series of NW-trending faults (USGS, 2019). On July 5th, 34 hours after the initial M_w 6.4 foreshock, at 8.19 pm PST the M_w 7.1 mainshock occurred ~15 km north of the foreshock epicenter, and ruptured mostly bilaterally along a NW-trending dextral fault system for a total length of ~50 km. The rupture termination of the mainshock in the south occurred ~4.5 km north of the Garlock fault, and in the north terminated within the Coso volcanic field, a region of diffuse fracturing.

The 2019 Ridgecrest earthquake sequence has been imaged by a suite of optical and radar sensors which have acquired detailed measurements of the surface deformation at various spatial resolutions and sensitivities to ground displacement. These include, radar interferometry from ESA's Sentinel-1 and JAXA's ALOS-2, terrestrial and aerial lidar, drone photogrammetry and satellite optical imagery (e.g., WorldView, Sentinel-2 and Pleiades), as well as campaign and continuous GPS (Chen et al., 2019; Donnellan et al., 2019; Fielding et al., 2019; Funning et al., 2019; Hudnut et al., 2019; Xu et al., 2019). Although these data will provide measurement of surface deformation in remarkable spatial detail, they do not offer sufficient temporal resolution to separate the ground deformation of the closely timed foreshock and mainshock events. Here we present a relatively new class of high-resolution optical satellite imagery from the commercial satellite company Planet labs (with 3-m ground sampling distance), which due to its unique daily revisit time capability allows us to measure changes in the co-seismic surface displacement field through the Ridgecrest sequence. Imagery from this cubesat constellation have been used previously with image correlation techniques to study surface changes to study river ice floes, glacier migration, and earthquake deformation (Bao et al., 2019; Kääb et al., 2017, 2019). Here we present and apply a new image correlation technique called OR-Corr (Outlier-Resistant Correlator), that we have developed that provides a more stable correlation results that is less sensitive to outliers than standard image correlation methods. We apply this correlation approach to the daily Planet Labs imagery which allows us to separate the surface deformation of the closely-timed foreshock and mainshock events and measure the amount of fault displacements. These types of optical imagery which we provide here can be used to help validate and guide field survey mapping, provide constraints for finite fault slip inversion models to better resolve and separate slip at depth between these events and calculate the redistribution of stresses which may have triggered the mainshock.

First, we describe the acquisition parameters of the images acquired before, between and after the foreshock-mainshock sequence and their sources of noise. We then describe the new subpixel correlation technique that we have developed and apply this to the optical imagery to quantify the amount of horizontal ground deformation and magnitude of fault slip for each event. We then create difference maps from the pre- and post- foreshock, mainshock image pairs to define the temporal occurrence of fracturing and compare these to correlation and phase gradient maps from Sentinel-1 radar data. Finally, we then attempt to validate our results with imagery acquired by other optical and radar satellites.

Planet Labs Satellite Constellation

The constellation of satellites operated by the private entity Planet is composed of ~175 10 cm × 10 cm × 30 cm cubesats known as "Doves." These cubesats collectively acquire optical imagery over continental areas on a daily basis, providing a product known as PlanetScope imagery. The majority of the cubesats operate in a near-polar, sun-synchronous orbit of ~8° and ~98° inclination at an altitude of ~475 km, acquiring imagery from both ascending and descending orbits. The cubesats are optical frame cameras with the main sensor being a telescope and CCD area array, which collects 4-band imagery (RGB and near-infrared) at ~3-5 m resolution depending on the altitude. The PlanetScope images have a relatively narrow swath footprint of ~24.6 × ~16.4 km, and are acquired in near-nadir, with small variations of the look-angle in the across track direction of ~5° (Planet Team, 2019). The cubesats are frame camera systems which acquire instantaneously in one acquisition position, which is in contrast to more typical push-broom acquisition modes which collect images line-by-line as the sensor array scans across the width of the swath sequentially in the orbital direction. This difference of the cubesat image acquisition mode leads to different distortions that will become apparent when attempting to validate our surface deformation results from the PlanetScope imagery with ESA's Sentinel-2 optical push-broom satellite.

PlanetScope Imagery

We used a total of 33 Planet Scope images with 3-m resolution that are the level 3B product, which are orthorectified images that comes with radiometric, sensor and geometric corrections. The sensor corrections include removal of optical distortions caused by the sensor optics and co-registration of bands, where the lens model is known to have an accuracy of a fraction of a pixel (better than 0.1) (Kääb et al., 2019, Planet Team, 2019). Radiometric corrections are applied to the images using a mixture of calibration coefficients determined before launch and during orbit using on-board calibration techniques. The orthorectification of the images corrects for topographic distortions using the best available DEM (with posting ranging from 30 to 90 m), and are coregistered using other available optical imagery (including aerial imagery, RapidEye and Landsat 8), with ground control points (which provides the mapping between the reference and warp images) located using a combination of phase correlation and mutual information techniques (Planet Labs, 2019). To assess the quality of the surface deformation maps derived from the PlanetScope imagery and the effects of these corrections, we compare them to similar image correlation results derived from Sentinel-2 optical data (10 m pixel resolution), and correlation and phase gradient maps from repeat-pass Sentinel-1 radar, the latter of which characterizes the disturbance of the surface spectral properties (see Xu & Sandwell (in prep) for details).

In total we correlated 25 pairs of images across the foreshock and mainshock events, where 12 of the images used for correlation were acquired from before the foreshock, eight images between the foreshock and mainshock (with five collected on July 4th and three collected on July 5th), and 13 after the mainshock, (see Fig. 2 and Table 1 for details of dates). 29 of the images were captured at 11.13 am and four between 17.12-18.14 pm PST (for the descending and ascending tracks, respectively). We have made these orthoimages freely available for download from GeoGateway (http://geo-gateway.org/main.html).

Image correlation method

To measure the 2D horizontal surface deformation we used a sub-pixel correlation algorithm applied to the before and after optical images. We use a similar image correlation approach of

(Debella-Gilo and Kääb, 2011) in the spatial domain, which is applied to a stack of the three visible bands. The correlation method we have developed first calculates the Spearman rank correlation coefficient between image pairs to determine displacement at the integer level. We then fit a Gaussian function to the correlation function to determine its peak that defines the amount of sub-pixel motion. The Spearman rank correlation coefficient (ρ_w) is a nonparametric measure of the rank correlation, which correlates the *n* ranks of two random variables (in this case a subset of the before (*x*) and after (*y*) images), rather than the values of the variables themselves (i.e., the pixel values). Otherwise the correlation calculation (eq. 1) is similar to the Pearson correlation coefficient, which is the covariance of the ranks of the images (C_{xy}, eq. 2, where C is the covariance matrix) normalized by the product of their standard deviations (σ, eq. 3, where $\bar{x}_w$ is the weighted mean, eq. 4).

$$\rho_w = \frac{C_{xy}}{\sigma(x)\sigma(y)} \quad 1)$$

$$C_{xy} = \frac{\sum_{i=1}^{N} w_i(x_i - \bar{x}_w) \cdot w_i(y_i - \bar{y}_w)}{\sum_{i=1}^{N} w_i} \quad 2)$$

$$\sigma(x) = \sqrt{C_{xx}} \quad 3)$$

$$\bar{x}_w = \frac{\sum_{i=1}^{N} w_i x_i}{\sum_{i=1}^{N} w_i} \quad 4)$$

In the correlation scheme we impose a Gaussian weighting (*w*) to the pixels within the correlation window, so that pixels located at the center are weighted higher than those at the edges. We use the Spearman rank as it is more resistant to outliers than a standard Pearson correlation coefficient when correlating patches of the images as the values of the outliers are limited to their rank value and as such we have named our correlation algorithm OR-Corr (Outlier-Resistant Correlator).

Outliers may arise between the images due to changes from vegetation, building damage, or urban development and we have found our approach produces more stable results in such regions. For the deformation maps provided here we used correlation windows with dimensions of 33 × 33 pixels with a step size of 29 pixels, which results in a correlation map of 87 m resolution. In total we produced 12 correlations for the foreshock and 13 for the mainshock, where we correlated each image sub-swath separately due to the spatial overlap between image pairs which allows for more reliable corrections of long-wavelength artifacts that we describe next.

Both the north-south and east-west deformation maps show long-wavelength (> 5 km) artifacts that are up to ~0.7 pixel (~2 m) in amplitude (Fig. S1). To correct for these we fit and remove quadratic and ramp functions, which we assume reflects errors in the original camera sensor correction and mis-registration, respectively. This correction reduces the root-mean square (RMS), of the foreshock deformation maps by 41% and 89% in the east-west and north-south directions, respectively, and 42% and 91% for the mainshock deformation maps. Following removal of the long-wavelength artifacts from the deformation maps we then stack the separate correlation results using a uniform weighting. We do not use all of the individual correlation results to produce the final correlation result (Fig. 3), as some exhibit large topographic artifacts, or have unusually large noise levels which we could not correct for (see Table 1 for which image pairs were used), which likely results from large differences in incidence angles between the images. After stacking we then apply a median filter (3 × 3 pixels) that helps reduce noise in the deformation maps.

Image Correlation Results

The horizontal deformation maps separated for the foreshock and mainshock (fig. 3a and 3b, respectively) captures primary surface faults with large displacement (> 20 cm). For the foreshock-only deformation map only the main NE-striking left-lateral rupture strand can be distinguished. In contrast, the mainshock only deformation maps show the primary rupture strand and other major NW striking secondary faults along the central segment of the rupture. In both deformation maps, smaller wavelength artifacts exist such as linear features caused by roads which are translationally invariant features (i.e., their spectral pattern looks similar across different regions), and topographic artifacts resulting from use of a single DEM to orthorectify the images, that assumes no advection of topography has occurred. These deformation maps can be used to help constrain the magnitude of shallow fault slip (< 5 km depth) in fault slip inversion models, and are useful in that they can separate the contribution of ground deformation due to slip at depth, which is important for accurately forward calculating Coulomb stress changes and for understanding the possible triggering effect of the foreshock to the surrounding faults (e.g., Chen et al., 2019; Xu, et al., 2019).

To measure the fault slip distribution from the deformation maps we used profiles orientated perpendicular to the fault strands, that stacks the surface motion in the fault-parallel direction. We first project the surface motion from the north-south and east-west directions that are output from the correlation into the fault trace direction. The fault offsets are then measured using profiles with lengths of 7 km and stacked over widths of ~1.5 km. The total fault-parallel displacement is calculated as the total amplitude of the offset across the fault-zone (Fig. 4), and are provided as a supplementary data file. The fault displacement measurements provide an estimate of how surface slip varies along the rupture and the overall slip distribution. The slip profile of the foreshock shows an asymmetric shape that is skewed to the southwest, and has an average displacement of 0.56 m ± 0.10 (standard error), and a maximum of 0.89 ± 0.11 (1-σ). For the mainshock slip profile we find a sample mean of 1.68 ± 0.19 m (standard error) and a maximum of 3.92 ± 0.38 m (1-σ). We note the maximum slip value we observe is in good agreement with the maximum value documented from field survey observations (currently reported to range from 4.1-4.5 m, black marker shown in Fig. 4 (Kendrick et al., 2019)).

Uncertainty Analysis of Deformation Maps

Due to noise in the resulting deformation maps, surface fractures of smaller displacement are not detected. To understand the threshold of observable displacement, we calculate the precision and spatial correlations using the sample semi-variogram and covariogram, respectively (Chilbs and Delfiner, 2000; Sudhaus and Sigurjón, 2009). Constraining the error structure is also useful for incorporating these data into finite-fault slip inversions in order to generate meaningful and consistent weights when used jointly with other datasets e.g., InSAR or GPS. In addition, the empirical covariances can be used to generate sets of synthetic data errors that can be added to perturb the observations and through a series of inversions derive distributions of the modeled fault slip parameters (e.g., Sudhaus and Sigurjón, 2009). To estimate the error variance and autocovariances we use a subset of pixels in a far-field stable region that are presumed to contain minimal tectonic deformation. This implies the error is stationary and that the error structure of the chosen region is representative of the rest of the deformation measurements. The semi-variogram and covariogram are estimated as half the average squared difference and half the mean product between points separated at distances h, respectively (Fig. 5). The data variance is estimated at the sill point, where the semi-variogram plateaus at distances larger than the correlation length, which we report as the standard deviation in eq. 5 and 6 at h = 0, which we found was similar for the foreshock (1σ = 20 cm) and mainshock (1σ = 15 cm) deformation maps. To provide a continuous description of the spatial dependence of the covariances we fit the sample covariogram with an exponential model of the form shown in (eq. 5 and 6, and shown in Fig. 5).

$$C_{fore}(h) = \begin{cases} 20\ cm, & for\ h = 0 \\ 212 \cdot e^{-\frac{h}{549}}, & for\ h > 0 \end{cases} \qquad 5)$$

$$C_{main}(h) = \begin{cases} 15\ cm, & for\ h = 0 \\ 87 \cdot e^{-\frac{h}{280}}, & for\ h > 0 \end{cases} \qquad 6)$$

To assess the accuracy of the deformation maps and fault offsets we compare them to measurements derived from correlation of Sentinel-2 optical imagery, which covers both the foreshock and mainshock events (06/28/19-07/18/19) (Fig. S2). Although the Sentinel-2 deformation maps have horizontal, across-track striping artifacts resulting from jitter of the spacecraft during the push-broom type acquisition of the images which we have attempted to correct for, we find an overall good agreement with the PlanetScope result (Fig. 4). The slip profiles have a very strong agreement in the overall magnitude and shape of the slip distribution as shown by correlation coefficient of 0.95, giving confidence the PlanetScope imagery provides robust estimates of the surface fault displacement for each event.

Resolving Surface Disturbance

The PlanetScope images that separately bracket the foreshock and mainshock allows for assessment of which faults ruptured when. In addition to applying optical image correlation to measure the ground displacement, we also analyzed the before-and-after images themselves and calculate pixel-by-pixel differences between them, where the latter helps constrain areas of surface disturbance. Although image correlation has the ability to resolve sub-pixel shifts between images, the minimum resolvable displacement is limited by the radiometric noise (caused primarily by thermal noise of the CCD array) and biases associated with orthorectification (where the variances are provided in eq. 5 and 6). Difference maps can instead be useful for directly determining disruption of the surface caused by fractures of smaller differential motion that may not be detected by the image matching technique. In addition, another advantage of difference maps is that they are applied at the pixel level which gives a result at the full image resolution that can help resolve smaller scale details of fracturing that the spatially coarser deformation maps may miss (the final correlation resolution is determined by the window skip size which is 29 pixels, or 87 m in this case).

Visual inspection of just the post-foreshock July 4^{th} optical image (i.e., that shown in Fig. 2 b) shows new NE trending fractures directly east of the city of Ridgecrest traversing the 178 highway and into the China Lake Naval Air Weapons Station military base. However, to better isolate the fractures from the images, we compute the difference between the before and after images which helps highlight changes of the surface that could be produced where new scarps cause shadows or distributed fracturing causes changes in the surface texture (Fig. 6). We note that caution must be made in interpreting the difference maps as these include any changes that have occurred between the image acquisitions including, rockfalls and landslides along steep topographic gradients, shadows along topographic lineaments (although we expect this to be small as the maximum time span of the difference maps are mostly 1-2 weeks), water spillage due to pipe leakages, sand boils and liquefaction. To help understand whether the lineations found in the difference maps are tectonic, we compare them to correlation and phase gradient maps from Sentinel-1 radar amplitude images, which characterizes changes to the coherence of surface spectral properties and gradients of the phase in the satellite look directions respectively, and current (but not complete) field mapping observations (Kendrick et al., 2019). We note all of the supporting Sentinel-1 radar data are not able to distinguish the timing of deformation between the foreshock and mainshock events, but are useful to check of the location of fractures that we interpret from the difference maps.

The difference maps spanning just the foreshock period clearly delineate the primary trace of the foreshock rupture, which is continuous for ~10 km in a NE direction. The difference maps also clearly show a parallel NE-striking, 5.5 km long fracture that is located ~1.8 km directly north of the primary M_w 6.4 rupture strand. Interestingly, south of the primary foreshock rupture strand we observe a 3 km by 2.5 km wide zone of distributed fracturing that seems to be from a distinctly different fault zone from the primary foreshock rupture. Although, we note surface disturbance in this area could also reflect possible effects from sand boils and liquefaction. At the southwestern most termination of the foreshock there are a series of fractures that form a NNW trending 2.5 km long fracture that is conjugate and almost perpendicular to the foreshock rupture trace. At the foreshock-mainshock intersection the location of the foreshock rupture becomes less clear and possibly splays out. Unfortunately, determining any possible interaction of the foreshock faults with the mainshock at this intersection is not possible due to the coarseness of the image resolution. Northeast of the foreshock-mainshock intersection there is NE-striking fracturing that is distributed over a 4.5 km by 5 km wide region. We note that these short fault segments traverse multiple NW trending dykes, that from the pre-foreshock imagery clearly show previous offsets, indicating the foreshock in this area had ruptured along pre-existing faults.

The difference maps that span the just mainshock period (Fig. 6b) show a clear, mostly single-stranded NW-trending rupture trace along the central section near the foreshock-mainshock intersection. However, it becomes more difficult to follow the rupture trace either farther south or north towards both rupture terminations. This could be a result of i) a decrease of the overall amount of displacement, ii) the rupture becoming increasingly more diffuse towards the rupture terminations, and/or iii) the strike of the rupture at the terminations becomes almost parallel with the illumination direction (115.4º), producing a less pronounced shadow and therefore less pronounced signal in the difference maps than the NNW-SSE striking central rupture section which is more oblique to the illumination direction. We note that we do not observe any re-rupture of the foreshock strands during the mainshock, indicating most if not all of the deformation observed along the NE-trending foreshock fractures occurred during the foreshock. Qualitatively comparing the rupture fabric (or width) between the foreshock and mainshock ruptures, the difference maps clearly show the foreshock is distinctly more complex in its geometry (excluding sites where the mainshock rupture intersects with other secondary macroscopic faults), suggesting it is a more immature fault system (Wesnousky, 1988).

From analysis of the images and difference maps we have provided a .kmz of fracture mapping as a supplementary dataset, which we have classified into fractures that occurred during the foreshock or mainshock. Our fracture mapping dataset is then further classified into high or low confidence features. Fractures of high confidence are expressed as clear linear features in both the difference maps and the optical images, and do not coincide with topography or possible changes in shadows. Fractures of low confidence are features that appear as diffuse, quasi-linear features in the difference maps and optical images, or are coincident with topography and possible shadowing. We note that there are fractures observed by field surveys that are not included in our fracturing mapping dataset. Such instances mostly occur in areas of high relief where topographic artifacts and shadows may have masked any surface changes that occurred due to fractures, and an absence of these features in our mapping dataset does not necessarily suggest that our interpretation is that they did not occur in either the foreshock or mainshock events (e.g., by pre or post-seismic fracturing). In addition, it is more difficult to discern fractures orientated in the NW direction, as the sun illumination direction is almost parallel to these fractures (azimuth of 115.4° on July 5th at 11.20 am PST), which produces minimal shadows and therefore little signal in the image difference maps. Therefore, it is slightly more difficult to provide complete rupture mapping associated with the mainshock (mostly faults striking NW), than the foreshock (orientated NE and almost perpendicular to the illumination direction).

To validate our fracture mapping from the optical images and difference maps we compare these to field survey mapping made in the days-weeks following the ruptures, and correlation and phase gradients from Sentinel-1 radar data. The field data were gathered by a collective team of field geologists including the USGS, CGS, and other academic institutions (Kendrick et al., 2019). We processed the radar correlation and gradient maps from a pair of descending Sentinel-1 images using GMTSAR, with the correlation maps estimated as the correlation co-efficient between the before (07/04/2019) and after (07/28/2019) amplitude maps, and gradient maps processed using the method of Sandwell and Price (1998), which has the advantage of avoiding unwrapping errors. Overall, we find very good qualitative agreement of the fracture locations imaged between these different datasets (Fig. 6 and 7). However, in some areas there seems to be clear fracturing observed in the optical difference and radar correlation maps but not in the field data, which suggests that there are likely additional sites still to be ground-truthed. The fracture mapping from just the radar correlation and phase gradients can be found as a .kmz file in the supplementary dataset.

Summary

The 2019 Ridgecrest earthquake sequence poses several interesting questions including, what triggering mechanism(s) could explain the occurrence of the widespread secondary fractures surrounding both surface ruptures, and how was the mainshock rupture triggered by the foreshock sequence? To help understand these problems we have provided data and analysis of optical images acquired by the Planet Lab cubesat constellation. The data acquired by this platform are distinct from other geodetic imaging datasets (e.g., InSAR, lidar or aerial photos) in that they acquired images between the foreshock and mainshock events, allowing discrimination of which fractures occurred when and with how much surface displacement. Here we describe products derived from these images including, difference maps, fracture mapping and horizontal surface deformation maps from subpixel image correlation. These datasets have potential use for constraining slip inversion models and the calculation of static stress changes associated with the foreshock and its effect on faults that later ruptured during the mainshock (e.g., Chen et al., 2019), and assessment of its relative importance compared to other possible triggering mechanisms such as poroelastic, aseismic postseismic and dynamic stress changes.

Data and Resources

All of the derived data products presented in this analysis can be downloaded from the Zenodo data repository (http://doi.org/10.5281/zenodo.3546342). This includes the difference maps (Fig. 6), the Planet Labs correlation maps (Fig. 3), kmz files of the fracture mapping, Sentinel-1 gradient maps that was processed here (where additional results processed by David Sandwell's group at UCSD, Scripps can be found at https://topex.ucsd.edu/SV_7.1/index.html), Sentinel-1 correlation maps (where additional SAR data can be downloaded from ARIA, https://aria-share.jpl.nasa.gov/20190704-0705-Searles_Valley_CA_EQs/Interferograms/), and the fault offsets illustrated by the along-strike slip profile (Fig. 4). GMTSAR and ISCE can be downloaded by a number of package managers, see http://gmt.soest.hawaii.edu/projects/gmt5sar/wiki for installation instructions. The Sentinel 1 and 2 imagery can be downloaded from ESA's open access data hub from (https://scihub.copernicus.eu/) and Alaska's Satellite Facility UAF (https://www.asf.alaska.edu/) [07, 2019]. The figures were made using Generic Mapping Tools (Wessel and Smith, 1991) and QGIS (https://qgis.org/en/site/forusers/download.html). MATLAB is available at www.mathworks.com/products/matlab (last accessed August 2019). GDAL, which was used for some of the image processing, can be freely downloaded through most library package managers. Supporting information contains the corrections to the correlation results (S1) and optical image correlation result from Sentinel-2 (S2), used to compare the slip distribution shown in Fig. 4.

Acknowledgements

We would like to thank Tom Rockwell and Steve DeLong for their suggestions that helped improve the manuscript. We would also like to thank Saif Aati, Ken Hudnut, Katherine Kendrick, Kate Scharer, Eric Xu, and Gordon Seitz for helpful discussions. **Funding**. Part of this research was supported by the National Aeronautics and Space Administration, and performed at the Jet Propulsion Laboratory, California Institute of Technology under contract with NASA. Funding for this project was provided under a National Postdoctoral Program fellowship to C. Milliner administered by the Universities Space and Research Association through a contract with the National Aeronautics and Space Administration and NASA's Earth Surface and Interior program. We also thank Planet Labs for access to their archive of imagery which was instrumental to this study which helped guide the field survey response for rupture mapping.

References

Bao, H., Ampuero, J.-P., Meng, L., Fielding, E.J., Liang, C., Milliner, C.W.D., Feng, T., Huang, H., 2019. Early and persistent supershear rupture of the 2018 magnitude 7.5 Palu earthquake. Nat. Geosci. 12, 200–205. https://doi.org/10.1038/s41561-018-0297-z

Chen, K., Avouac, J., Aaati, S., Milliner, C., Zheng, F., & Shi, C. (2019, 08). Cascading, pulse-like ruptures during the 2019 Ridgecrest earthquakes, East California Shear Zone. Poster Presentation at 2019 SCEC Annual Meeting.

Chilbs, J.-P., Delfiner, P., 2000. Geostatistics. Technometrics 42, 444–444. https://doi.org/10.1080/00401706.2000.10485746

Debella-Gilo, M., Kääb, A., 2011. Sub-pixel precision image matching for measuring surface displacements on mass movements using normalized cross-correlation. Remote Sens. Environ. 115, 130–142. https://doi.org/10.1016/j.rse.2010.08.012

Donnellan, A., Lyzenga, G. A., Parker, J. W., Ansar, A., Goulet, C. A., Ben-Zion, Y., Vernon, F. L., & Lynch, D. K. (2019, 08). Targeted High-Resolution Topographic Imaging of

Active Faults and the Ridgecrest Earthquake Sequence Ruptures in Southern California. Poster Presentation at 2019 SCEC Annual Meeting.

Dziewonski, A.M., Chou, T.-A., Woodhouse, J.H., 1981. Determination of earthquake source parameters from waveform data for studies of global and regional seismicity. J. Geophys. Res. Solid Earth 86, 2825–2852. https://doi.org/10.1029/JB086iB04p02825

Fielding, E. J., Stephenson, O., Zhong, M., Sangha, S. S., Liang, C., Huang, M., Liu, Z., Yun, S., Simons, M., & Brooks, B. A. (2019, 08). SAR Imaging of the Coseismic and Early Postseismic Deformation from the 2019 Mw 7.1 and Mw 6.4 Ridgecrest Earthquakes in California. Poster Presentation at 2019 SCEC Annual Meeting.

Funning, G., Floyd, M., & Terry, R. L. (2019, 08). Distinguishing slip from the M6.4 and M7.1 Ridgecrest earthquakes using campaign GPS data. Poster Presentation at 2019 SCEC Annual Meeting.

GEER, 2019. Preliminary Report on Engineering and Geological Effects of the July 2019 Ridgecrest Earthquake Sequence. https://doi.org/10.18118/g6h66k

Hudnut, K. W., Brooks, B. A., Scharer, K. M., Hernandez, J. L., Dawson, T., Oskin, M. E., Arrowsmith, R., Blake, K., Bork, S., Boggs, M., Glennie, C. L., Fernandez-Diaz, J., Singhania, A., & Hauser, D. L. (2019, 07). Airborne lidar and electro-optical imagery along surface ruptures of the 2019 Ridgecrest earthquake sequence, southern California. Poster Presentation at 2019 SCEC Annual Meeting.

Kääb, A., Altena, B., Mascaro, J., 2019. River ice and water velocities using the Planet optical cubesat constellation. Hydrol. Earth Syst. Sci. Discuss. 1–20. https://doi.org/10.5194/hess-2019-62

Kääb, A., Altena, B., Mascaro, J., 2017. Coseismic displacements of the 14 November 2016 Mw 7.8 Kaikoura, New Zealand, earthquake using the Planet optical cubesat constellation. Nat. Hazards Earth Syst. Sci. 17, 627–639. http://dx.doi.org/10.5194/nhess-17-627-2017

Kendrick, K. J., Akciz, S. O., Angster, S. J., Avouac, J., Bachhuber, J. L., Bennett, S. E., Blake, K., Bork, S., Brooks, B. A., Burgess, P., Chupik, C., Dawson, T., DeFrisco, M. J., Delano, J., DeLong, S., Dolan, J. F., DuRoss, C. B., Ericksen, T., Frost, E., Gold, R. D., Graehl, N. A., Haddon, E. K., Hatem, A. E., Hernandez, J. L., Hitchcock, C., Hudnut, K. W., Koehler, R. D., Kozaci, O., Ladinsky, T., Madugo, C. M., Mareschal, M., McPhillips, D., Milliner, C., Morelan, A. E., Nevitt, J., Olson, B., Padilla, S. E., Patton, J. R., Philibosian, B., Pickering, A., Pierce, I., Ponti, D. J., Pridmore, C., Rosa, C., Roth, N., Scharer, K. M., Seitz, G. G., Spangler, E., Swanson, B. J., Thomas, K., Thompson Jobe, J., Treiman, J. A., Williams, A. M., & Oskin, M. E. (2019, 08). Geologic observations of surface fault rupture associated with the Ridgecrest M6.4 and M7.1 earthquake sequence by the Ridgecrest Rupture Mapping Group. Poster Presentation at 2019 SCEC Annual Meeting.

McClusky, S.C., Bjornstad, S.C., Hager, B.H., King, R.W., Meade, B.J., Miller, M.M., Monastero, F.C., Souter, B.J., 2001. Present day kinematics of the Eastern California Shear Zone from a geodetically constrained block model. Geophys. Res. Lett. 28, 3369–3372. https://doi.org/10.1029/2001GL013091

Planet Team. Planet Data Application. Program Interface: In Space for Life on Earth. San Francisco, CA, USA. Available online: https://api.planet.com (accessed on July 6th 2019).

Rockwell, T.K., Lindvall, S., Herzberg, M., Murbach, D., Dawson, T., Berger, G., 2000. Paleoseismology of the Johnson Valley, Kickapoo, and Homestead Valley Faults:

Clustering of Earthquakes in the Eastern California Shear Zone. Bull. Seismol. Soc. Am. 90, 1200–1236. https://doi.org/10.1785/0119990023

Sandwell, D.T., Price, E.J., 1998. Phase gradient approach to stacking interferograms. J. Geophys. Res. Solid Earth 103, 30183–30204. https://doi.org/10.1029/1998JB900008

SCEDC (2013), Southern California Earthquake Center. Caltech Dataset. doi: 10.7909/C3WD3xH1

Sudhaus, H., Sigurjón, J., 2009. Improved source modelling through combined use of InSAR and GPS under consideration of correlated data errors: application to the June 2000 Kleifarvatn earthquake, Iceland. Geophys. J. Int. 176, 389–404. https://doi.org/10.1111/j.1365-246X.2008.03989.x

U.S. Geological Survey, 2019, Earthquake Data System: U.S. Geological Survey database available online at https://earthquake.usgs.gov/earthquakes/. (Accessed July 10th, 2019).

Wesnousky, S.G., 1988. Seismological and structural evolution of strike-slip faults. Nature 335, 340–343. https://doi.org/10.1038/335340a0

Wessel, P., Smith, W.H.F., 1991. Free software helps map and display data. Eos Trans. Am. Geophys. Union 72, 441–446. https://doi.org/10.1029/90EO00319

Xu, X., Ward, L. A., Smith-Konter, B. R., Milliner, C., Fang, P., Bock, Y., & Sandwell, D. T. (2019, 08). Surface rupturing and triggered slip on nearby faults from the Ridgecrest earthquakes revealed by InSAR. Poster Presentation at 2019 SCEC Annual Meeting.

Xu, X., Sandwell, D. T., Co-seismic displacements of the 2019 Ridgecrest earthquake sequence revealed by Sentinel-1 InSAR: small scale deformation near the rupture (in prep), Seismological Research Letters, Data Mine Article.

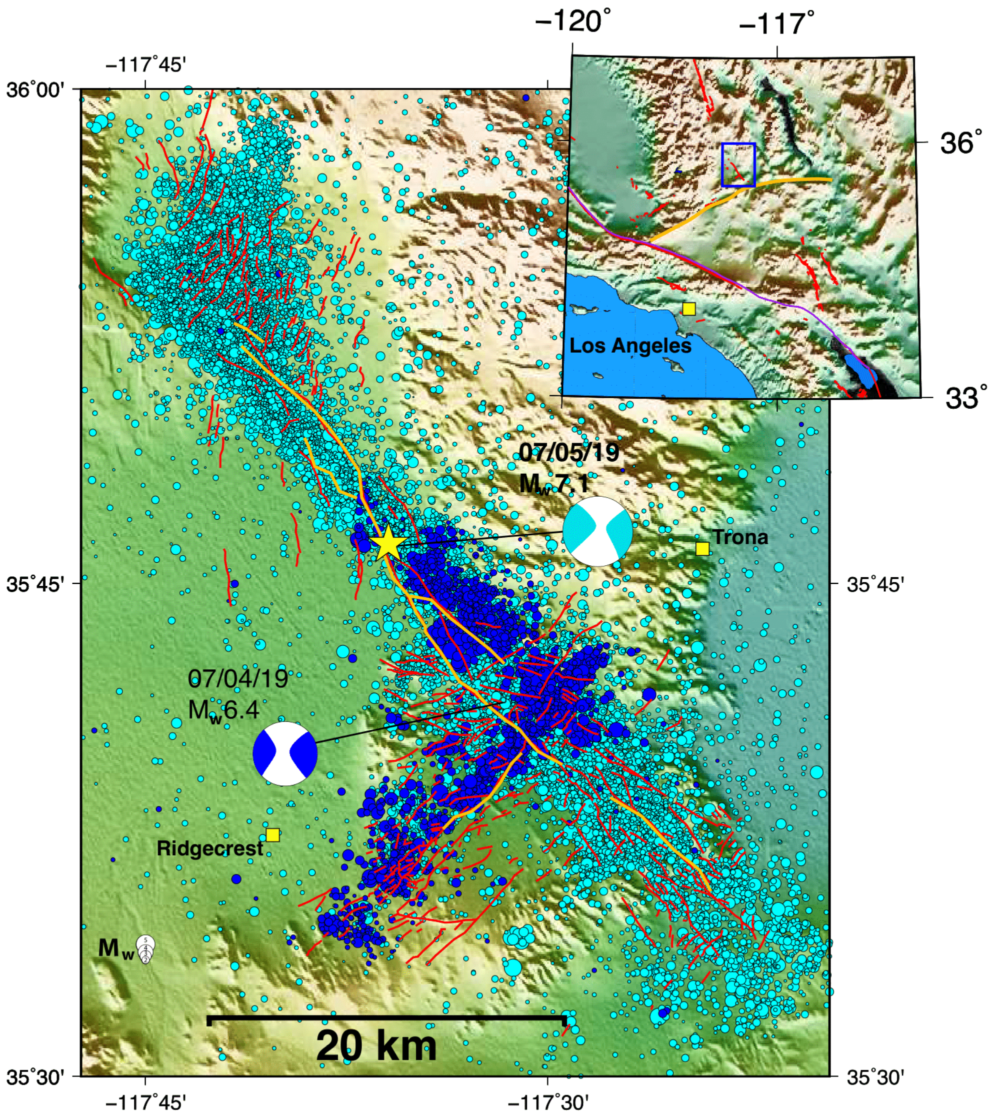

Fig. 1. Overview of the 2019 Ridgecrest earthquake sequence. Inset map shows the location of the Ridgecrest event within the Eastern California Shear Zone, CA, with historical events shown by red lines (https://earthquake.usgs.gov/hazards/qfaults/), and the Garlock fault by the orange

line. Main figure, the M_w 6.4 July 4th foreshock focal mechanism is shown in dark blue with seismicity that occurred following this and before the M_w 7.1 mainshock on July 5th, 17.12 pm PST (shown as the cyan focal mechanism) (Dziewonski et al., 1981), shown as dark blue circles with size indicating magnitude (SCEDC, 2013). Cyan circles show aftershocks following the mainshock event. Orange lines show fault traces of the foreshock and mainshock rupture mapped from optical image correlation (Fig. 3), and red lines mapped from Sentinel-1 correlation and gradient maps (Fig. 6 c, d). For faults mapped separately for the mainshock and foreshock see Fig. 2b and c, 6, 7 and the supporting .kmz dataset.

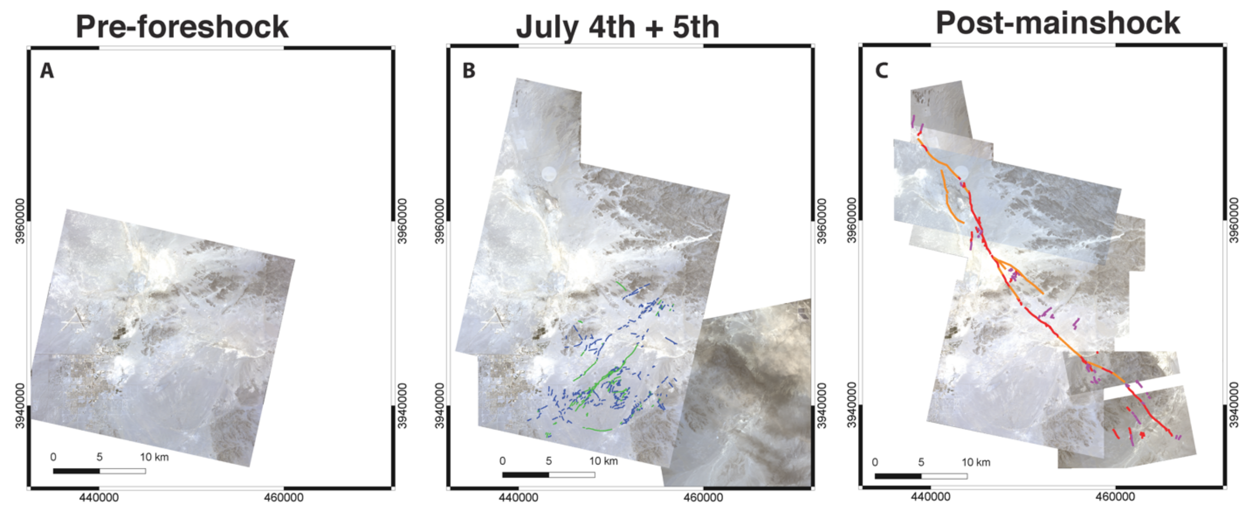

Fig. 2 Overview optical data from Planet labs used in this analysis. We used the 3-m orthorectified PlanetScope imagery acquired before (a), between (b), and after (c), the foreshock and mainshock events. For clarity we do not show all the imagery used prior to the foreshock in (a), but Table 1 details the number of images used.

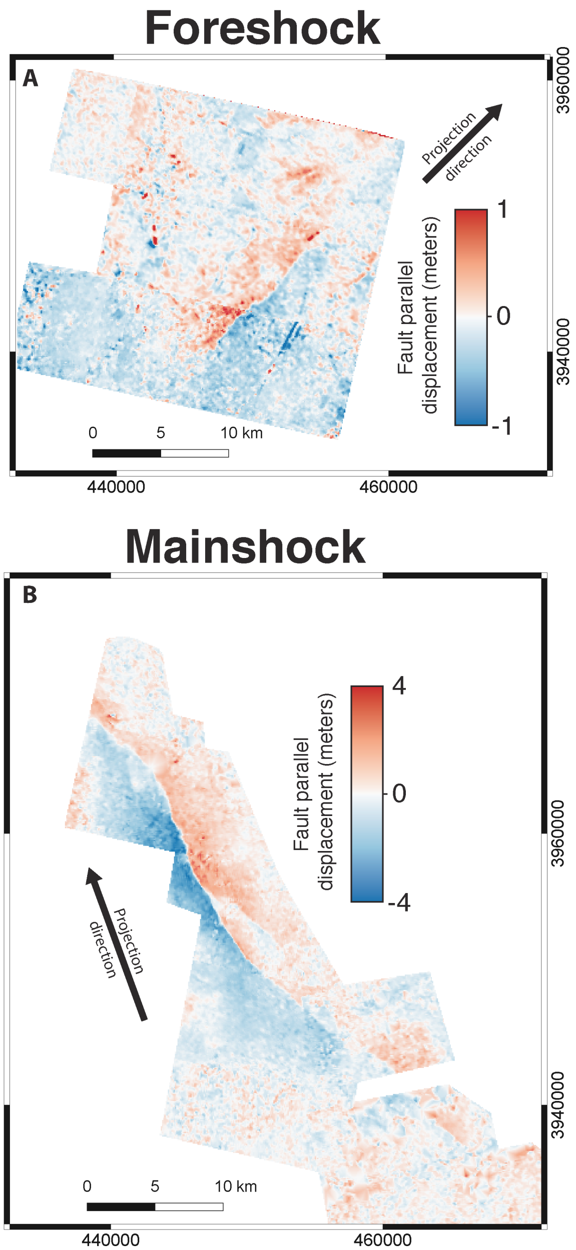

Fig. 3. Deformation maps showing surface motion projected into fault parallel direction (with direction shown by arrow) that are calculated from subpixel correlation of optical images shown in Fig. 2. a) top, shows deformation map from correlating images spanning just the foreshock, while b) shows the surface displacement estimated from images spanning just the mainshock.

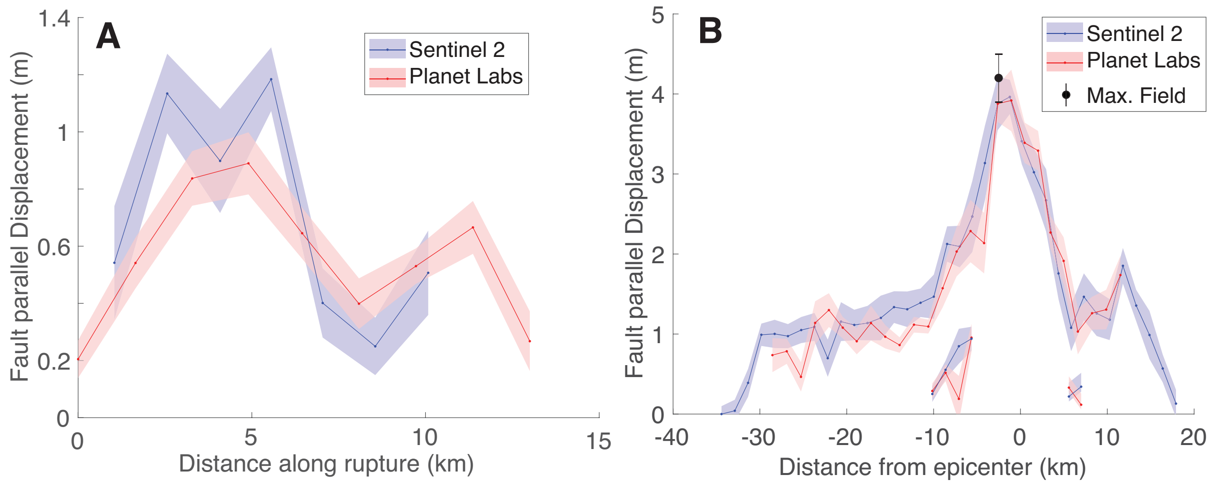

Fig. 4. Comparison of surface slip profiles for the foreshock (left) and mainshock (right), measured from the deformation maps from correlating PlanetScope and Sentinel-2 optical imagery with error bars denoting 1σ uncertainty (Fig. 3 and Fig. S2). Left, shows surface slip profile for just the foreshock (viewing NW). Right, shows surface slip profile for just the mainshock plotted as a function of distance from the epicenter, viewing SW. Correlation result of Sentinel-2 optical images is shown in Fig. S2, which contains both the foreshock and mainshock. The agreement in surface displacement amount between the two datasets indicates it is unlikely there was significant triggering or re-rupture of faults.

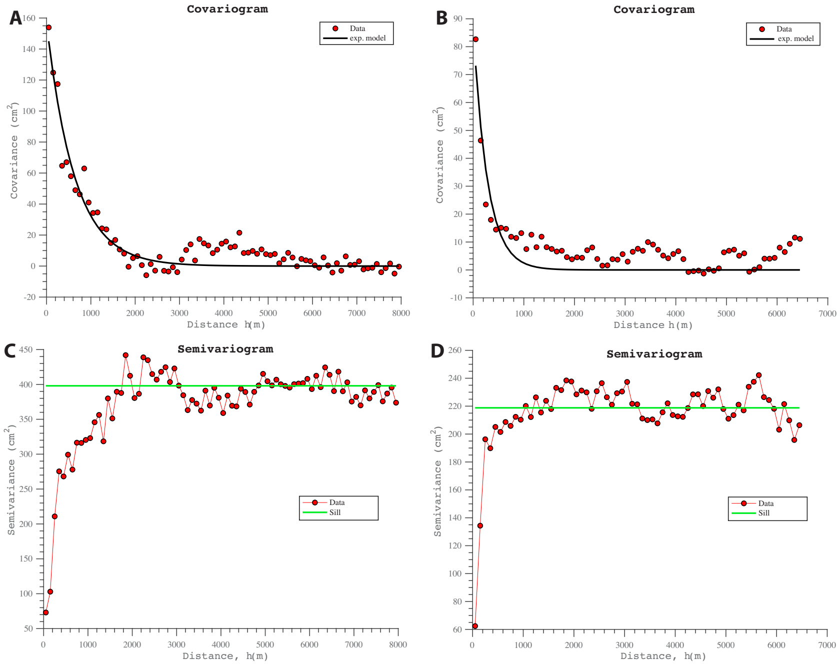

Fig 5. Error analysis of the deformation maps (shown in Fig. 3). Top row shows covariogram, bottom shows semivariogram of the foreshock (left column) and mainshock (right column) deformation maps. A) and b) are fit with an exponential model (black line) with coefficients shown in eq. 5 and 6 that provides a continuous description of the spatial dependence of the surface displacement measurements (red dots). While c) and d) provides an estimate of the data variance (green line) that is independent of the spatial correlations.

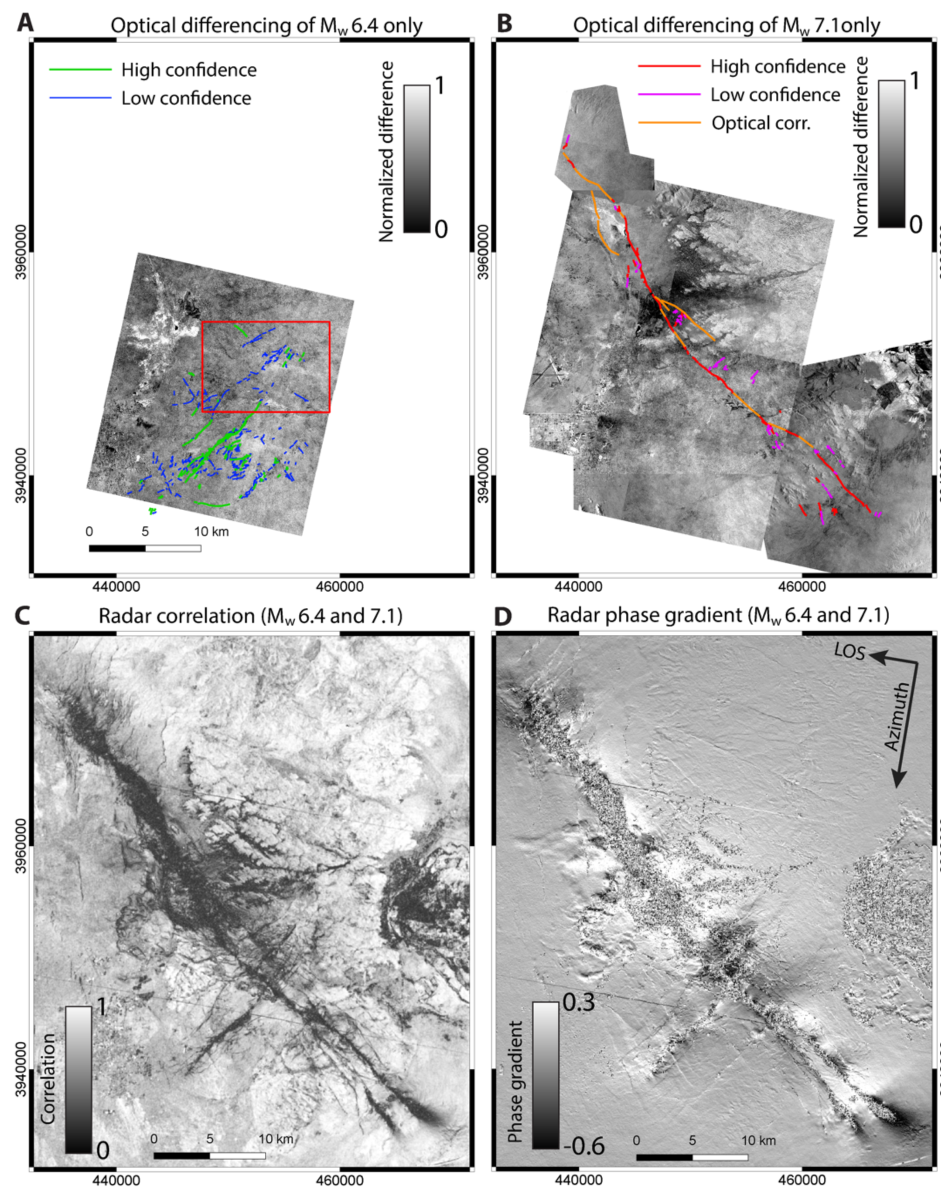

Fig. 6. Optical difference maps constraining the timing of surface disruption (top row), with analysis from Sentinel-1 radar data for comparison (bottom row). a) and b), show difference maps estimated from optical images spanning just the foreshock and mainshock, respectively. a) illustrates fault mapping interpretations shown as green and blue lines that are traces mapped with high and low confidence, respectively. b) Red, purple and orange traces indicate fractures mapped with high and low confidence, and those mapped from the optical correlation dataset (Fig. 3b), respectively. These fault traces and difference maps are available as a supplementary dataset. Red

box in a) shows location of Fig. 7. c) and d) show correlation of radar amplitude and phase gradient, respectively, from a pair of descending Sentinel-1 images. c) Dark areas show disruption to the surface, or changes in the spectral properties that cause decorrelation, while in d) discontinuities indicate areas of large gradients in the phase in the azimuthal direction, with units of radians per pixel (~30 m) and calculated using the method of Sandwell & Price (1998), also see Xu and Sandwell (in prep) for additional details.

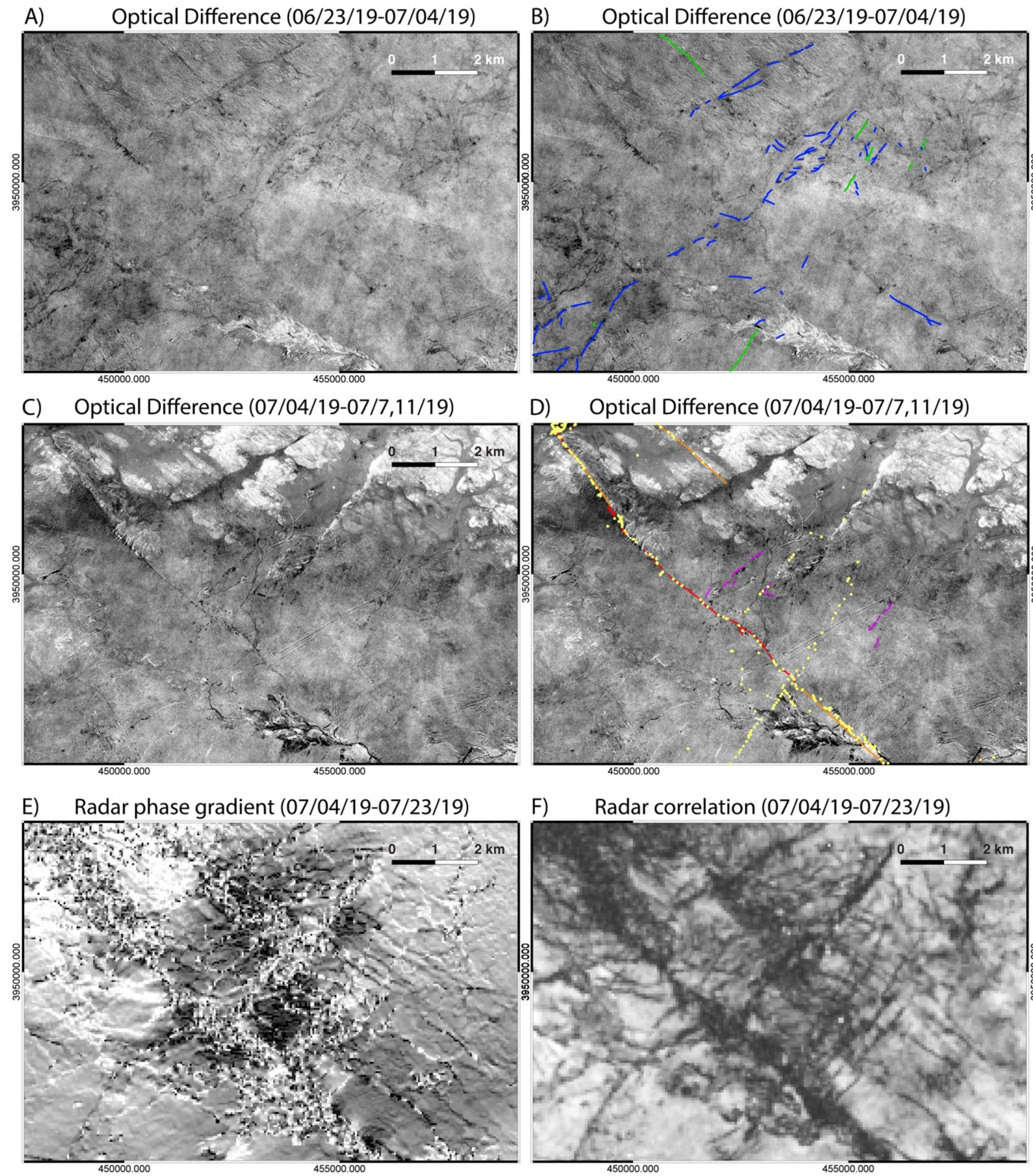

Fig. 7. Sequence of surface fracturing captured during the foreshock (top row), and mainshock (second row), around the area of the fault intersection. Top row shows difference maps from Planet labs generated from images spanning just the foreshock, where b) illustrates mapping interpretation of fractures, green and blue lines indicates traces that are of high and low

confidence respectively, values range are normalized differences and range from 0-1. c) and d) show difference maps from images spanning just the mainshock, with d) showing mapping interpretations with red, purple and orange colors indicating fractures mapped with high and low confidence, and those mapped from the optical correlation dataset (Fig. 3b), respectively. Yellow dots are observation points from field surveys of Kendrick et al. (2019). e) and f) show phase gradient and correlation results from descending Sentinel-1 (shown in Fig. 6c and d), respectively, which contains fracturing from both the foreshock and mainshock events.

Table 1 Acquisition times and number of subswaths of PlanetScope images used in foreshock and mainshock correlations.

Pre-Image	Post-Image	Foreshock (F), Mainshock (M)	Num. of subswaths used
05/13/19	07/04/19	F	2
06/07/19	07/04/19	F	3
06/20/19	07/04/19	F	2
06/30/19	07/04/19	F	2
07/01/19	07/04/19	F	3
07/04/19	07/06/19	M	4
07/04/19	07/07/19	M	1
07/04/19	07/11/19	M	3
07/04/19	07/11/19	M	1
07/05/19	07/08/19	M	2
07/05/19	07/14/19	M	2